

## Adam J. Smith

Department of Mechanical and Aerospace  
Engineering,  
Utah State University,  
4130 Old Main Hill,  
Logan, UT 84322  
e-mail: 12asmith3@aggiemail.usu.edu

## Hannah L. Maxwell

Department of Mechanical and Aerospace  
Engineering,  
Utah State University,  
4130 Old Main Hill,  
Logan, UT 84322  
e-mail: hannah.maxwell@usu.edu

## Hadi Mirmohammad

Department of Mechanical Engineering,  
University of Utah,  
201 Presidents' Cir,  
Salt Lake City, UT 84112  
e-mail: hadi.mirmohammad@utah.edu

## Owen T. Kingstedt

Department of Mechanical Engineering,  
University of Utah,  
201 Presidents' Cir,  
Salt Lake City, UT 84112  
e-mail: o.kingstedt@utah.edu

## Ryan B. Berke<sup>1</sup>

Department of Mechanical and Aerospace  
Engineering,  
Utah State University,  
4130 Old Main Hill,  
Logan, UT 84322  
e-mail: ryan.berke@usu.edu

# A Novel Variable Extensometer Method for Measuring Ductility Scaling Parameters From Single Specimens

*Macro-scale ductility is not an intrinsic material property but is dependent on the overall geometry of the specimen. To account for variety in specimen geometries, multiple ductility scaling laws have been developed, which scale ductility between different specimen sizes. Traditionally, these ductility laws rely on testing multiple different specimens of varying sizes to obtain material parameters, often done by varying gauge lengths. With the use of digital image correlation (DIC), this study presents a technique where multiple different gauge lengths are extracted from a single specimen to obtain ductility scaling parameters from a single experiment. This technique provides orders of magnitude more data from each specimen than previous techniques. This variable extensometer method is then validated by testing multiple different geometries, and select scaling laws are then compared.*

[DOI: 10.1115/1.4053034]

**Keywords:** ductility, scaling laws, digital image correlation, variable extensometer, mechanical properties of materials, plasticity

## 1 Introduction

As nuclear facilities age, it is critical to understand how materials degrade under irradiation conditions [1]. However, engineering-scale radioactive specimens are expensive to irradiate and difficult to handle [2]. A common area of concern for irradiated materials is the effect of reduced ductility [3]. Thus, there is a strong desire to develop techniques that can adequately characterize the effect of irradiation on ductility. Traditionally, ductility characterization is performed using engineering-scale tensile tests. However, testing of high-temperature and irradiated materials with this technique can present numerous safety and logistical challenges [2]. As such, there is significant interest in low-cost methods to characterize the ductility of materials. A common method is using miniaturized specimens, which experience less total radiation dose and are much safer to handle [4]. In recent years, several promising techniques have gained popularity (e.g., nano-indentation [5–7], micro-electro-mechanical-system based micro-tension [8–10], nano-pillar compression [11,12], or disk bend [2]). These techniques focus on measurements at a micro- or nanoscale and avoid macro-scale instrumentation. This has led to a significant gap in translating measurements at a micro- or nanoscale to material properties at an engineering scale.

Among other phenomena, ductility is affected by the grain size [13–15], temperature [16,17], and total radiation dose [18,19]. To understand how nuclear components will perform, it is necessary to characterize the ductility for each combination of environmental factors. However, ductility is also dependent on specimen geometry [20–23]. For example, in the late stages of ductility testing, localized necking means that two specimens of differing dimensions can produce drastically different elongation measurements [24]. Thus, it becomes necessary to use scaling laws to translate ductility measurements between different sized specimens. Among the oldest and most popular are Barba's Law [25] (developed in 1880) and Oliver's Law [26] (developed in 1928). Oliver's Law has become the standard scaling law used in ISO 2566-1:1984 [27] although it does have limitations. Takeda et al. demonstrated that Oliver's Law is not applicable to pure iron with a thickness between 0.2 mm and 2 mm due to the effect of stress triaxiality [20]. Chen et al. verified the applicability of both Oliver's and Barba's Law if the specimen aspect ratio was less than or equal to 9.89. The ISO 2566-1 states that Oliver's Law is not applicable to steels with a tensile strength over 700 MPa. However, Xu et al. addressed this by developing modifications to Oliver's Law for the use on high-strength pipeline steel by adding a term that was dependent on tensile strength [28].

Historically, ductility scaling parameters are found by testing multiple specimens of the same material having different combinations of gauge length and cross-sectional area. The parameters are then solved empirically by fitting a mathematical function to the data. This can be expensive and introduce safety hazards when testing high-temperature or irradiated specimens. One method to

<sup>1</sup>Corresponding author.

Contributed by the Applied Mechanics Division of ASME for publication in the JOURNAL OF APPLIED MECHANICS. Manuscript received August 28, 2021; final manuscript received November 13, 2021; published online December 7, 2021. Assoc. Editor: Yong Zhu.

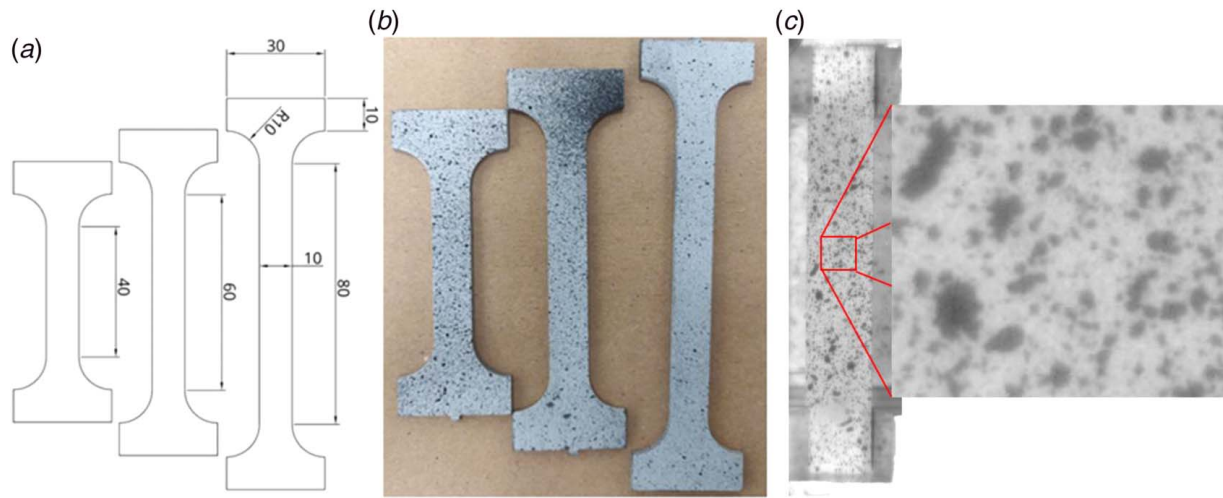


**Fig. 1** (a) Drawing of tensile specimens with 80 mm, 60 mm, and 40 mm gauge lengths used for testing, (b) photo of select specimens with applied speckle patterns, and (c) a specimen in the testing apparatus with a zoomed view of the speckle. All dimensions shown are in mm.

combat this was developed by Dhalla and Winter [29]. With the observation that the only criterion for gauge length is that it must encase the nonuniform elongation (i.e., necking), they marked multiple gauge lines every  $\frac{1}{4}$  in. along a 3 in. specimen. By measuring the total elongation between each pair of gauge lines post-mortem, they were able to obtain both Barba's Law and Oliver's Law parameters from a single specimen, thus reducing cost and time while improving safety. In this study, their technique is expanded upon through the development of a novel variable extensometer method to obtain ductility parameters using digital image correlation (DIC).

Digital image correlation is an image-based displacement measurement technique that offers several unique benefits that make it excellent for extracting multiscale ductility measurements. First,

it is a noncontact method capable of in situ measurements where conditions may prohibit contact measurements [30,31]. Second, it can be applied to different length scales limited only by the field-of-view and resolution of the camera [32,33]. Finally, it provides full-field data across the entirety of the specimen surface as opposed to the single-point strain of strain gauge or the total extension of a physical extensometer [34]. By leveraging these benefits, DIC can be used to apply many virtual extensometers, which track the extension between two points [35], thereby obtaining many simultaneous measurements of elongation.

In this article, a novel variable extensometer approach is presented, which uses DIC for the application to Barba's and Oliver's Laws. Under the technique, many virtual extensometers

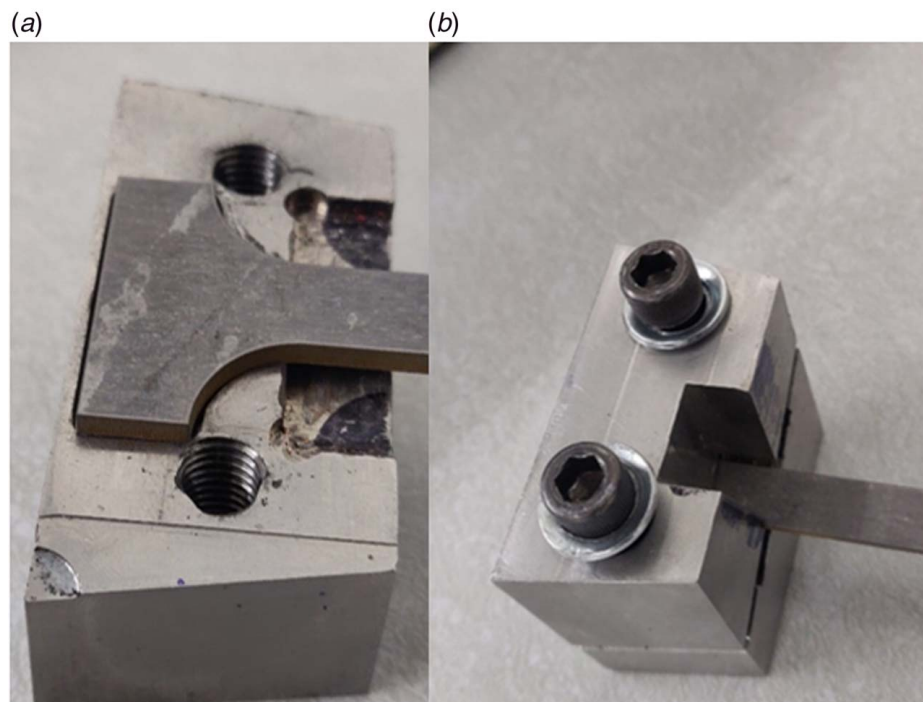


**Fig. 2** (a) Photo showing the specimen seated in the machined recess in the grips, and (b) photo showing the top part of the grip that clamps onto the specimen and holds it in place. The grips angle the specimen to match the viewing angle of the Gleeble window. A notch through the top part of the grip allows cameras to view more of the gauge length.

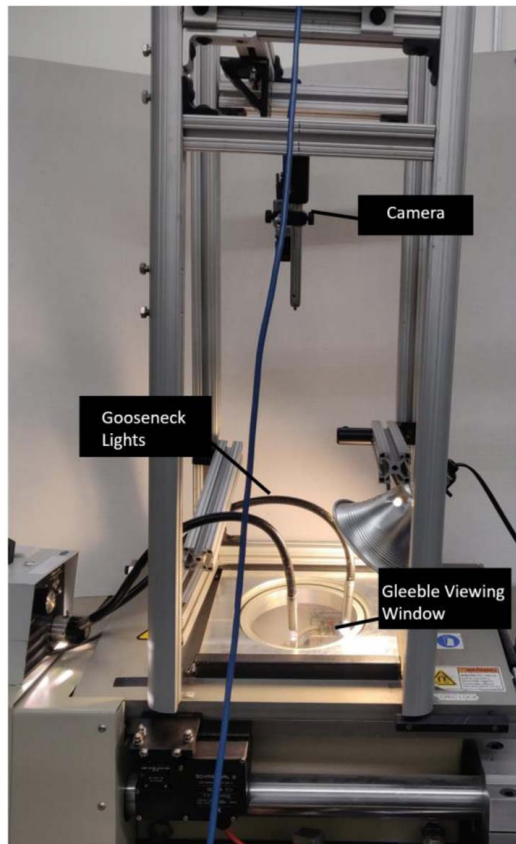


Fig. 3 Placement of camera and lighting over the viewing window of the Gleeble test chamber

are extracted from 2D DIC data by varying gauge length across the length of the specimen, thereby allowing for the determination of ductility scaling parameters from a single specimen. In this study, low carbon steel dog-bone tensile specimens with gauge lengths of 80 mm, 60 mm, and 40 mm are tested and compared to validate the technique. The results show that the variable extensometer technique can accurately extract ductility scaling while providing more data than is available from traditional methods. In addition, a comparison is made comparing the performance of the scaling laws using this technique.

## 2 Methods

Specimens were machined out of low carbon A36 steel sheet 2.5 mm thick with a constant 10 mm gauge width ( $A_0 = 25$  mm) using a computer numerical control (CNC) water jet with dimensions shown in Fig. 1. A total of nine specimens were machined: three with an 80 mm gauge length, three with 60 mm, and three with 40 mm. The specimens were then speckled for DIC using VHT high-temperature spray paint with a white background and a black speckle as shown in Fig. 1(b).

The specimens were loaded using a Gleeble 1500 D thermomechanical simulator, which consists of a load frame with a joule heater inside of an environmental chamber. The environmental chamber of the Gleeble includes a viewing window through which to allow for image-based measurements to be taken during testing [36,37]. To match the angle of the viewing window, specimens were placed in stainless steel grips machined to orient the specimen surface at an angle parallel to the viewing window. The grips contain a recess that matches the shoulders of the specimen, and the top half of the grips clamps down on the top with two  $\frac{1}{4}$ -20 bolts as shown in Fig. 2. The grip-to-grip displacement was measured using a linearly varying displacement transducer.

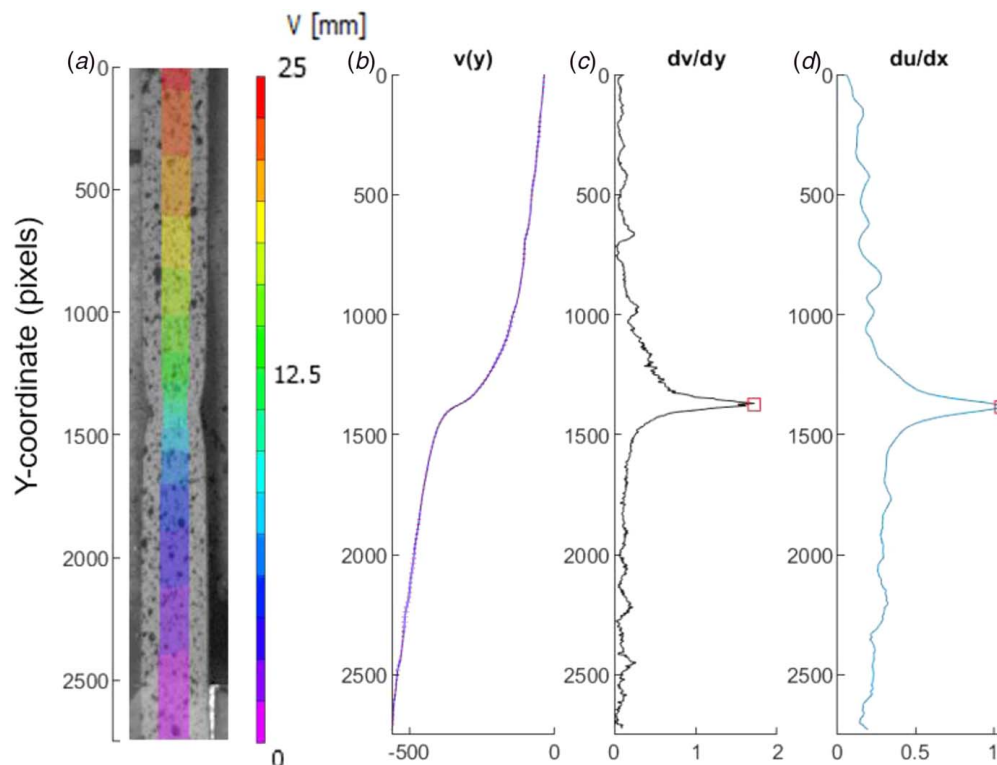
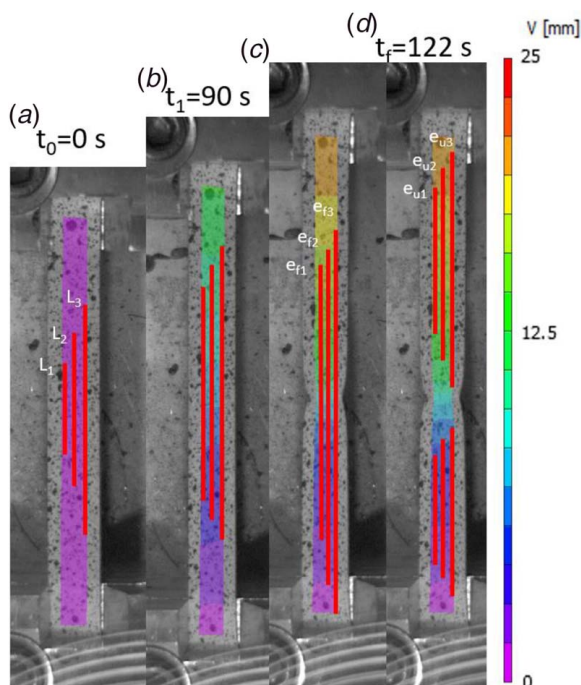


Fig. 4 Plots used for identifying the necked region. (a) The DIC contour giving of the vertical displacement in mm, (b) the vertical displacement in terms of pixels  $v(y)$  along the length of the specimen, (c) the change in vertical displacement  $dv/dy$  along the length of the specimen, and (d) the change in horizontal displacement  $du/dx$  across the width of the specimen.





**Fig. 5 Demonstration of the variable extensometer process. (a)** A reference image at time  $t=0$  is used to obtain original gauge lengths,  $L_0$ , for many simultaneous virtual extensometers, which span both sides of the necked region. **(b)** The displacement of each extensometer increases over time as the specimen elongates. **(c)** The final image before failure is used to compute the elongation at failure,  $e_f$ , for many simultaneous extensometers. **(d)** Virtual extensometers that do not span the necked region are instead used to obtain many simultaneous measurements of the uniform elongation,  $e_u$ . Note that to avoid overlapping of the three gauges, this schematic shows the three gauge lines at different horizontal positions, but the true measurements use averaged 1D displacements of the type shown in Fig. 4(b).

The specimens were additionally monitored throughout testing by use of a 15.1 MP Basler ace camera (Exton, PA) equipped with a 25 mm fused quartz lens from Universe Kogaku (Oyster Bay, New York) as shown in Fig. 3. Although the Gleeble system is capable of testing at high temperature, all tests were performed at room temperature. Specimens were deformed in tension

under displacement control at a rate of 0.125 mm/s until fracture. This translates to strain rates of  $0.0016 \text{ s}^{-1}$  for the 80 mm specimen,  $0.0021 \text{ s}^{-1}$  for the 60 mm specimen, and  $0.003 \text{ s}^{-1}$  for the 40 mm specimen. Images were captured at a rate of 2 Hz during of the test. DIC was performed using vic-2D v.6.2.0, a DIC software from Correlated Solutions (Irmo, SC), with a subset size of  $125 \times 125$  pixels and a step size of 5 pixels. Although the exact resolution varied between specimens, the 80 mm specimen used in the next few figures had a resolution of approximately  $2.9 \mu\text{m}/\text{pixel}$ .

**2.1 Step 1: Identifying the Necked Region From Digital Image Correlation Results.** The first step in performing the variable extensometer technique is to find the pixel location of the necked region along the length of the specimen. This was accomplished through examination of both the horizontal and vertical displacement throughout the length of the specimen, as demonstrated in Fig. 4. Figure 4(a) shows the vertical displacement contour ( $v$ , in mm) obtained shortly before failure from a specimen having an 80 mm gauge length. In Fig. 4(b), all subsets having the same  $y$ -coordinate (in pixels) are averaged together to reduce noise, and the results are then plotted as a function of  $y$ -position. The necked region exhibits an abrupt change in slope as the necked area displaces more drastically compared to the rest of the specimen. Figure 4(c) shows the slope  $dv/dy$ , which shows a distinct peak at the center of the gauge region, indicating the location where the specimen ultimately breaks. This peak is confirmed using slope of the change in lateral displacement,  $du/dx$ , obtained through a rolling average of the change in lateral displacement across the width of the specimen. The value obtained for each row of subsets is plotted along the length of the specimen shown in Fig. 4(d).

**2.2 Step 2: Applying Virtual Extensometers.** The center of the necked region is identified using the peaks of Figs. 4(c) and 4(d). The width of the necked region is then approximated by the regions of rapid slope change in each of these figures. For all specimens, the estimated necked region is between 200 and 250 pixels in length depending on the specimen. To ensure that pixels that contain the necked region are excluded from all extensometers, all subsets within 150 pixels on either side of the break are excluded from further analysis. To avoid potential stress non-uniformity caused by the grips, all subsets with 50 pixels of each end of the specimen were also excluded. All remaining  $v$ -displacements are averaged across the width of the specimen and paired against all other  $v$ -displacements to form many thousands of virtual extensometers. Pairs that span the break are used to compute two parameters, as demonstrated in Fig. 5. First, using

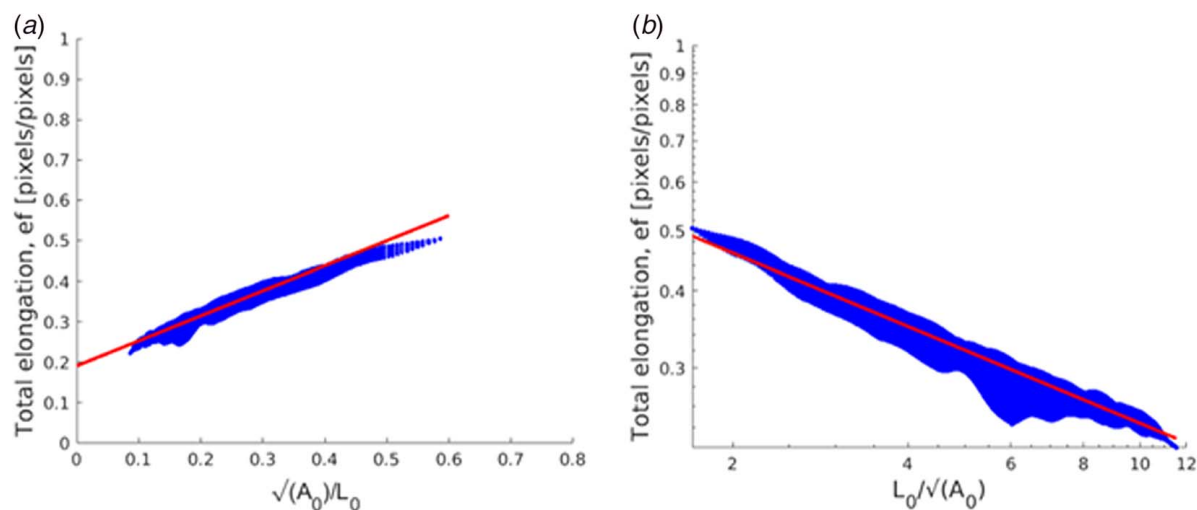


**Fig. 6 Variable extensometer data showing (a)  $e_f$  versus  $\sqrt{A_0}/L_0$  with Barba's Law fit overlaid and (b)  $e_f$  versus  $L_0/\sqrt{A_0}$  in logarithmic space with Oliver's Law fit overlaid**

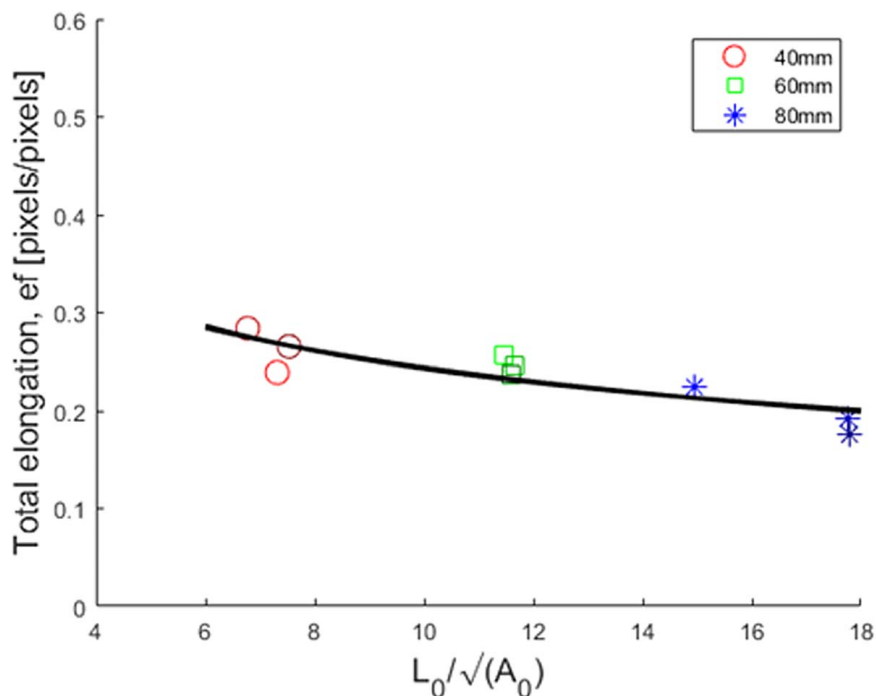


Fig. 7 Specimen-averaged data from each of the nine specimens, overlaid with the fitted expression for the unified law in Eq. (3)

the initial reference image as demonstrated in Fig. 5(a), the distance between each subset in the pair is used to compute the original gauge length for each extensometer,  $L_0$ . As the specimen elongates over time, the distance between subsets increases as demonstrated by the contour in Fig. 5(b). In the final image before failure, the distance between paired subsets is then used to compute the elongation at failure,  $e_f = \Delta L/L$ , as demonstrated in Fig. 5(c). This allows many simultaneous calculations of  $e_f$  for many gauge lengths  $L_0$ . The exact number of simultaneous

extensometers varied depending on the placement of the break, but the example in Fig. 5 included 55,454 measurements. Pairs that lie entirely on one side of the break are instead used to compute many simultaneous measurements of uniform elongation,  $e_u$ , as demonstrated in Fig. 5(d).

**2.3 Step 3: Generating Ductility Scaling Parameters.** With the extensometer values extracted, the many combinations of  $L_0$

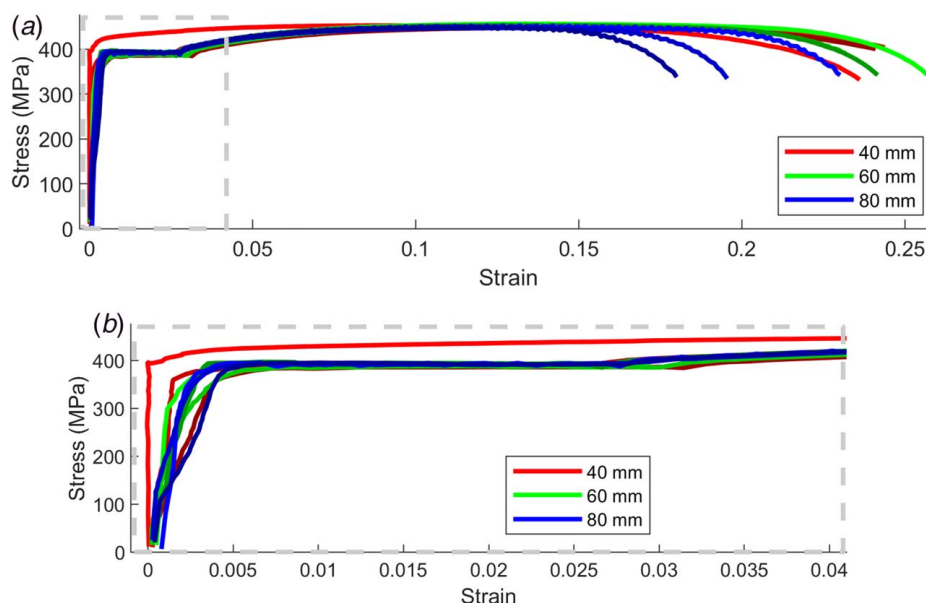
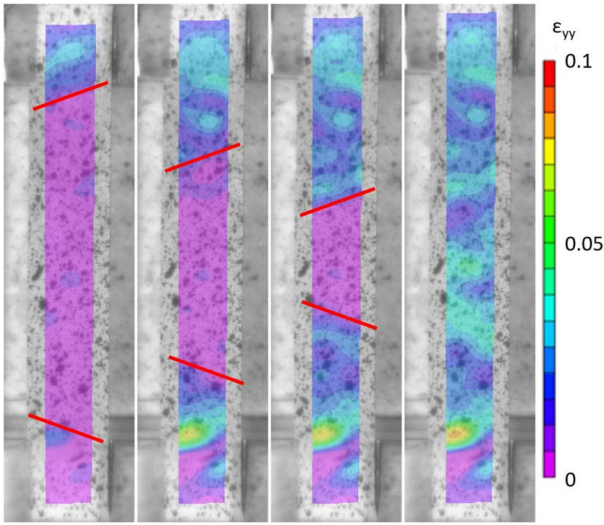


Fig. 8 Stress-strain curves for each of the nine specimens. (a) The full stress-strain curves and (b) only the portion contained by the dashed lines in (a). The 40 mm specimens are shown in varying shades of red, the 60 mm in shades of green, and the 80 mm in shades of blue. The strain comes from the camera measurement at 2 Hz, and the stress comes from the Gleeble force measurement at 60 Hz. (Color version online.)



**Fig. 9** Lüder's Bands observed in a 60 mm specimen. DIC strain contours in the vertical direction are shown overlaid on four sequential images. Red lines highlight the nonuniformity of the deformation as the specimen transitions from fully elastic (left) to fully plastic (right). (Color version online.)

and  $e_f$  are plotted on common axes to generate large point clouds as demonstrated in Fig. 6. Each point represents a unique combination of  $L_0$  and  $e_f$  from thousands of virtual extensometers, all obtained from the same specimen.

The point clouds are then fitted against three scaling functions using the "fit()" method in MATLAB. This function allows the use of anonymous functions where a function coefficients, variables, and constants can be defined. Starting points are provided that were obtained through a linear regression for Barba's Law, a logarithmic regression for Oliver's, and using the values obtained from Barba's and Oliver's Law for the Unified Law. The "fit()" method provides the values for the coefficients, the uncertainty, and the goodness-of-fit parameters.

The first is Barba's Law [25]:

$$e_f = \beta \frac{\sqrt{A_0}}{L_0} + e_u \quad (1)$$

where  $A_0$  is the original cross-sectional area of the specimen and  $\beta$  is a unitless scaling parameter that is solved for empirically. For large values of  $L_0$ , the contribution of the necked region becomes negligibly small, and  $e_f$  approaches  $e_u$ .

The second function is Oliver's Law [26]:

$$e_f = \kappa \left[ \frac{L_0}{\sqrt{A_0}} \right]^\alpha \quad (2)$$

where  $\kappa$  is a unitless scaling parameter (analogous to  $\beta$  in Eq. (1)) and  $\alpha$  is a unitless exponent, both of which are solved for empirically. For large values of  $L_0$  and negative  $\alpha$ ,  $e_f$  decays to 0.

It is worth noting that, compared to Barba's Law, the ratio  $L_0/\sqrt{A_0}$  is inverted in Oliver's Law. For a point cloud plotted on axes of  $\sqrt{A_0}/L_0$  and using a linear scale as they are plotted in Fig. 6(a), the Barba's Law function is linear with slope  $\beta$  and y-intercept  $e_u$ . For a point cloud plotted on logarithmic axes of  $L_0/\sqrt{A_0}$  as they are plotted in Fig. 6(b), the Oliver's Law function is linear with slope  $\alpha$  and intercept  $\log(\kappa)$ . The two equations can be combined into one unified law:

$$e_f = \kappa \left[ \frac{L_0}{\sqrt{A_0}} \right]^\alpha + e_u \quad (3)$$

This expression reduces to Barba's law when  $\kappa = \beta$  and  $\alpha = -1$ , or to Oliver's Law when  $e_u = 0$ .

**2.4 Other Benchmark Comparisons.** As a benchmark, the variable extensometer method is compared to the more historically used technique recommended in ISO 2566-1:1984 [27]. Under the technique, a single specimen-averaged measurement is obtained for each specimen by extracting  $e_f$  and  $L_0$  using the longest virtual extensometer, yielding a single data point for each specimen. The points are then plotted on a common axis, and the MATLAB "fit()" function is then applied to this data to compute ductility scaling parameters. This process is shown in Fig. 7.

Finally, although the variable extensometer technique can be applied independently to point clouds from all nine specimens, it is also applied a tenth time to a point cloud consisting of the combined dataset from all nine specimens.

### 3 Results

The engineering stress-strain curves for all nine specimens are shown in Fig. 8. The 40 mm specimens are shown in varying shades of red, the 60 mm in shades of green, and the 80 mm in shades of blue. Stress for each specimen is computed by dividing the force measured via the load cell by the original cross-sectional area,  $A_0$ . Strain for each is measured using the outermost virtual extensometer obtained via DIC.

Eight of the nine specimens tested displayed Lüder's Bands, as exhibited by the plateau regions that occur shortly after the yield. Also known as slip bands, these are inhomogeneous deformation when the specimen transitions from elastic to plastic deformation. This is a well-known phenomenon that has been observed with several methods including DIC [38]. Examples of DIC contours that are obtained at the beginning, middle, and end of the plateau for one such specimen are shown in Fig. 9. The specimen that did not exhibit a plateau also exhibited a significantly higher yield strength, but the reason for this discrepancy is unknown.

The point clouds from all nine specimens are plotted in Fig. 10. For visible clarity, the 40 mm data set is plotted first in red, then the 60 mm in green, and then the 80 mm in blue. The gray data represents the other two specimen sizes in each plot. The data points used in Fig. 7 are also superimposed.

A plot summarizing the ductility parameters as obtained empirically is shown in Fig. 11. The top row gives the value for  $\kappa$ ; the second row shows the value for  $-\alpha$  ( $\alpha = -1$  for Barba's Law); and the third row shows the value for  $e_u$  ( $e_u = 0$  for Oliver's Law). The columns are the values obtained from the 40 mm, 60 mm, and 80 mm, and the combined data/nonvariable extensometer values, respectively. Each parameter is obtained by directly fitting Eqs. (1)–(3) using the MATLAB "fit()" function. The combined data from all specimens is computed in three ways: first, the average value is obtained by averaging each of the values obtained individually. All data are obtained by applying each respective law to the entire dataset of all nine specimens shown in Fig. 10. Traditional is obtained by applying each law to the nine data points obtained from the traditional method shown in Fig. 7.

In the case of the unified law in Eq. (3), this produced some cases for which  $e_u < 0$ , indicating that the uniform elongation is compressive when the total elongation is in tension. As such results have no physical meaning, the unified law is repeated a second time by first measuring  $e_u$  directly from extensometers, which do not span the necked region, subtracting  $e_f - e_u$ , and then by curve-fitting Oliver's Law for the remaining two parameters:

$$e_f - e_u = \kappa \left[ \frac{L_0}{\sqrt{A_0}} \right]^\alpha \quad (4)$$

This expression is mathematically identical to Eq. (3) except that  $e_u$  is measured directly instead of used as a fitting parameter.

It is worth noting that the revised version of the unified law could not be directly applied to the all data or traditional methods because each specimen has a different value of  $e_u$ . In these cases, the average

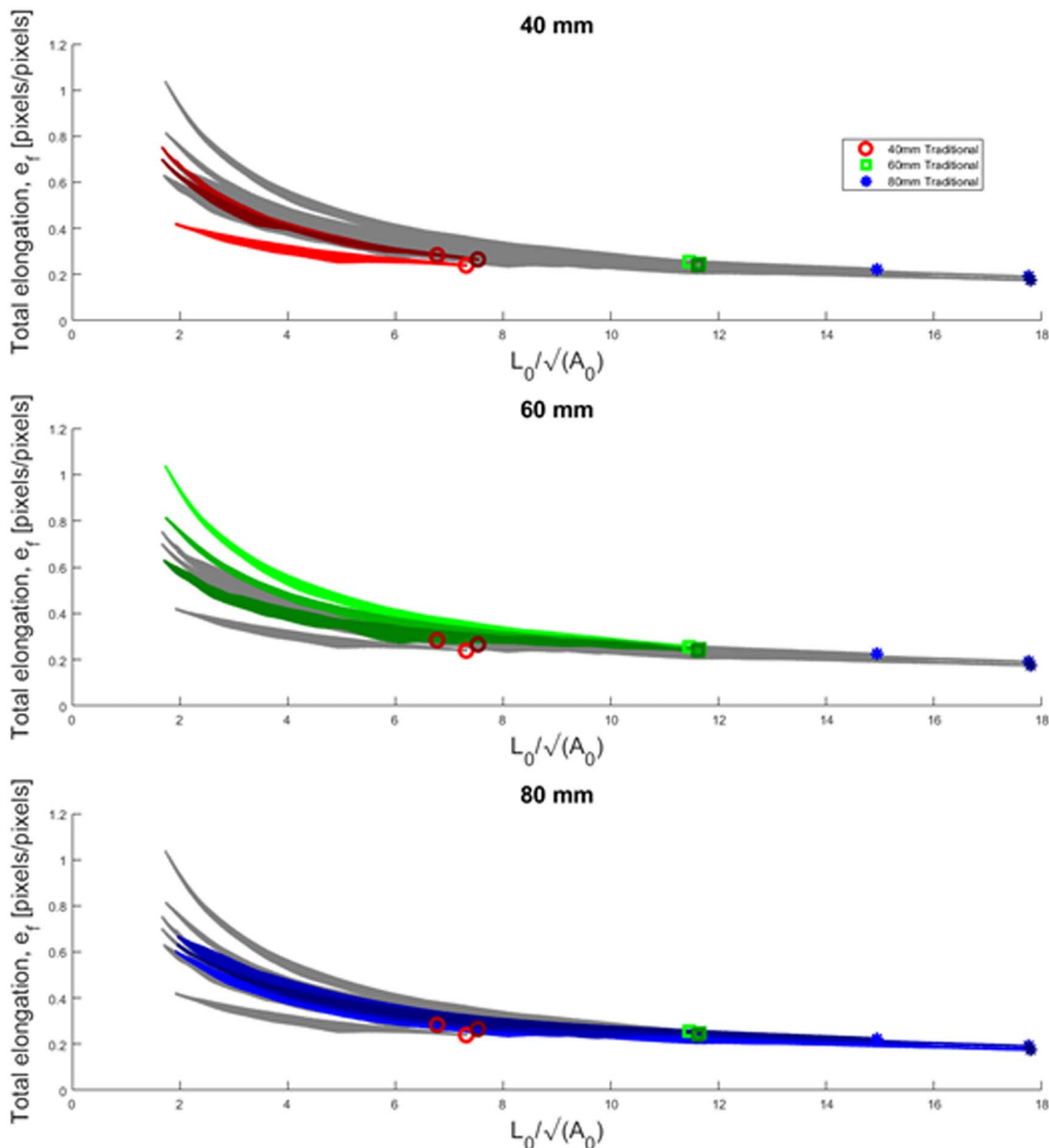


**Fig. 10** Point clouds obtained using the variable extensometer method for all nine specimens, with the top row emphasizing the 40 mm specimens in red, the middle row emphasizing the 60 mm specimens in green, and the bottom row emphasizing the 80 mm specimens in blue. The plots also include the nine specimen-averaged data points from Fig. 7.

value of  $e_u$  from the nine individual specimens is substituted instead.

#### 4 Discussion

The variable extensometer technique offers several advantages to the traditional method used for determining Barba's and Oliver's Law parameters. The first is that the parameters can be determined from a single specimen, which reduces testing time and cost. The technique also offers orders of magnitude more data, limited only by speckle size and camera resolution. This larger data set allows for much more robust statistical consideration of the properties

obtained from each specimen and comparison between specimens. The technique is not limited to use in Barba's and Oliver's Law and can be applied to other scaling laws that may be better suited for other materials other than were used in this study.

Further statistical consideration of the four laws is presented in Table 1. Three sets of data are presented, from left to right: the properties averaged from all nine specimens; the properties obtained from a point cloud of data from all nine specimens; and the properties obtained using a "traditional" fit to nine points obtained from the outermost extensometers from each of the nine specimens. This table also includes the 95% confidence intervals for each parameter, as well as the  $R^2$  value for each fit. It should be noted that the 95% confidence intervals of the "traditional" method are



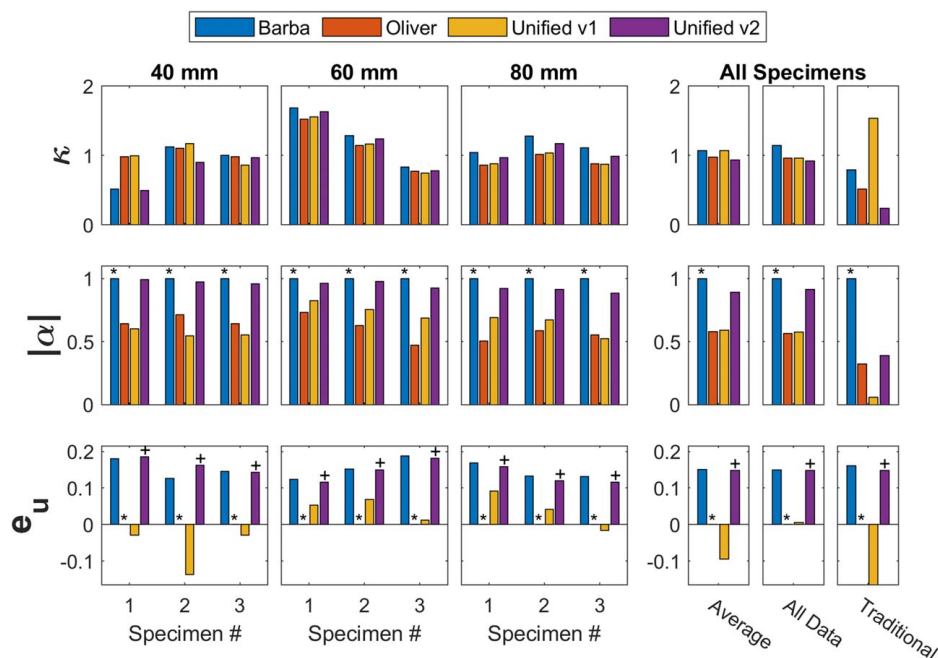


**Fig. 11 Summary of the ductility parameters obtained empirically from Eqs. (1) to (4). The asterisks (\*) indicate fixed values of  $\alpha = -1$  for Barba's Law and  $e_u = 0$  for Oliver's Law, which were assigned prior to fitting. The crosses (+) indicate values of  $e_u$  for Unified v2, which were measured directly prior to fitting. Note that for Unified v2, each specimen has a different values of  $e_u$ , so the value of  $e_u$  used to fit the combined datasets is the same as the value averaged from all nine specimens.**

very wide, such that the parameter values from all other methods fall comfortably within those bounds, but this is somewhat trivial because the bounds are so large. This is one of the drawbacks of the traditional method (and therefore a benefit of the new method): that due to statistical variability across specimens, it takes a very large sample population to obtain statistically meaningful measurements when there is only one measurement per specimen. Overall, the laws tend to agree that when  $e_u$  is not forced to be 0 (as in the case for Oliver's Law), then for this material,  $e_u$  tends to be on the order of about 0.15; and  $\alpha$  tends to be close to

1, indicating that for this material, Barba's Law remains a reasonable approximation.

In this study, there was relatively close agreement between (i) the property values found from each of the nine individual specimens, (ii) the average of each of those nine values, and (iii) the property values from a point cloud containing data from all nine specimens. This shows that the measurements are somewhat repeatable. Although some variability was seen across specimens, the variation across specimens having different geometry is comparable to or smaller than the variation within specimens having the same

**Table 1 Ductility parameters taken from the combined data set, the traditional method, and the average across each individual specimen with the 95% confidence interval,  $R^2$ , and the root mean squared error reported**

Law	Parameter	Specimen average		All data		Traditional	
		Value	95% Conf	Value	95% Conf	Value	95% Conf
Barba Eq. (1)	$\kappa$	1.0963	0.0040	1.1405	0.0041	0.7914	1.0189
	$e_u$	0.1498	0.0008	0.1499	0.0007	0.1604	0.1026
	$R^2$	0.974		0.8181		0.6584	
	RMSE	0.0097		0.0383		0.0215	
Oliver Eq. (2)	$\kappa$	1.0287	0.0024	0.9619	0.0033	0.5123	0.45498
	$A$	-0.6088	0.0015	-0.5651	0.0018	-0.3242	0.03761
	$R^2$	0.986		0.8295		0.7127	
	RMSE	0.0078		0.0373		0.0197	
Unified v1 Eq. (3)	$\kappa$	1.0463	0.0049	0.9617	0.0122	1.5387	207.96
	$\alpha$	-0.6557	0.012	-0.5746	0.0122	-0.0579	9.0720
	$e_u$	0.0059	0.0074	0.0057	0.0072	-1.1028	210.12
	$R^2$	0.98		0.829		0.712	
	RMSE	0.0071		0.0371		0.0205	
Unified v2 Eq. (4)	$\kappa$	1.0155	0.00481	0.9226	0.0069	0.24	0.9665
	$\alpha$	-0.9467	0.00513	-0.5746	0.0122	-0.39	1.74
	$e_u$	0.148	0.0119	0.148	0.0119	0.148	0.0119
	$R^2$	0.9785		0.6779		0.1553	
	RMSE	0.0068		0.0202		0.00339	



geometry. For example, in the top row of Fig. 11, the measured values of  $\kappa$  for the 40 mm and 80 mm specimens are relatively close to the mean value from all specimens, especially when compared to the first and last 60 mm specimens, which produce significantly higher and lower  $\kappa$ , respectively. This suggests that the variation in measurements is more likely the natural variation of the material and not a result of specimen dimensions.

This study also presents two versions of a new Unified Law, which combines Barba's and Oliver's Laws. This Unified Law is meant as an analytical tool—its only physical basis is the understanding that for very long specimens (i.e., the neck is negligibly short), Oliver's Law fails to account for  $e_u$  and instead decays to 0. Conversely, for very short specimens, Barba's Law fails to capture some nonlinearity at high aspect ratios of  $\sqrt{A_0}/L_0$ , as exhibited by point clouds such as Fig. 6(a).

Although Fig. 11 shows that the  $\kappa$  values produced by all four laws are roughly comparable, the first version of the Unified Law in Eq. (3) tended to produce  $\alpha$  and  $e_u$  values, which better agreed with Oliver's Law, while the second version in Eq. (4) tended to agree better with Barba's Law. In light of this observation, it is worth noting that Eq. (3) produced some  $e_u$  values that were positive and some that were negative, with an average near zero. This is clearly nonphysical, as when tension is applied to a tensile specimen, negative values of  $e_u$  would indicate that the un-necked portions of the specimen were somehow in compression. The second version corrects for this by measuring  $e_u$  directly before fitting for the remaining parameters. The measured  $e_u$  values agreed relatively closely with those fitted using Barba's Law, which seems to indicate that although Oliver's Law is much more recent compared to Barba's and is utilized in international ductility standards, its failure to correctly account for  $e_u$  makes Barba's Law worthy of further consideration.

It is worth noting that this analysis was performed using just a single material, A36 low carbon steel, which was purchased from a single vendor. The primary purpose of this article is not to present a new ductility law, and especially not one to apply to a broad range of materials. Rather, the purpose is to demonstrate a novel variable extensometer method for obtaining robust ductility parameters from single specimens. The results in Fig. 11 show that the measurements are repeatable across specimens, and the results in Table 1 show that they have much higher confidence compared to the traditional method, which uses one point per specimen. Further work is still needed to demonstrate the approach to other materials, more extreme variations in length scale, and to the incorporation of testing variables such as temperature and irradiation dose.

## 5 Conclusions

In summary, this study introduced a novel variable extensometer method to obtain ductility scaling parameters from single specimens. Using DIC, the variable extensometer extracts full-field, in situ displacement measurements across the entire gauge length of the specimen. The full-field displacements are then used to down-select many shorter gauge lengths over which to compute elongation by  $\Delta L/L_0$ . The many gauge lengths are validated by also comparing variable extensometer measurements from specimens having three different physical lengths: 40, 60, and 80 mm.

This technique was shown to have several benefits. First, it allows for ductility scaling parameters (e.g., the fitting constants from Barba's and Oliver's Laws) to be extracted from a single specimen. Second, by computing elongation thousands of times from each specimen, it provides orders of magnitude more data than previous techniques, which obtained one data point per failed specimen.

The variable extensometer technique allowed for further investigation of the two commonly used scaling laws: Barba's Law and Oliver's Law. A third, unified law was introduced by manually extracting  $e_u$  from the DIC data as an analytical tool to compare between the two laws. This investigation showed that the  $e_u$  obtained from Barba's Law was comparable to the manually

extracted  $e_u$ . By adding the manually extracted  $e_u$  constant to Oliver's Law, a unification of both laws was investigated. This unified law showed general agreement with Barba's Law.

## Acknowledgment

This study was supported by funding received from the DOE Office of Nuclear Energy's Nuclear Energy University Program (DOE-NEUP) under award No. DE-NE0008799. A. J. S. would also like to thank the US Department of Energy Office of Nuclear Energy for his graduate fellowship from the Integrated University Program. Any opinions, findings, conclusions, or recommendations expressed in this publication are those of the authors and do not necessarily reflect the views of the Department of Energy Office of Nuclear Energy. Portions of this work have been previously published under the MS thesis "Developing a Variable Extensometer Method for Measuring Ductility Scaling Parameters," by Smith [39].

## Conflict of Interest

There are no conflicts of interest.

## Data Availability Statement

The authors attest that all data for this study are included in the paper. No data, models, or code were generated or used for this paper.

## References

- [1] Lister, D. H., 2012, "Understanding and Mitigating Corrosion in Nuclear Reactor Systems," *Nuclear Corrosion Science and Engineering*, D. Féron, ed., Elsevier, New York, pp. 57–74.
- [2] Corwin, W. R., and Lucas, G. E., 1986, *The Use of Small-Scale Specimens for Testing Irradiated Material: A Symposium Sponsored by ASTM Committee E-10 on Nuclear Technology and Applications, Albuquerque, N.M., 23 Sept. 1983*, ASTM, Philadelphia, PA.
- [3] Kryukov, A., Debarberis, L., von Estorff, U., Gillemot, F., and Oszvald, F., 2012, "Irradiation Embrittlement of Reactor Pressure Vessel Steel at Very High Neutron Fluence," *J. Nucl. Mater.*, **422**(1), pp. 173–177.
- [4] Gussev, M. N., Howard, R. H., Terrani, K. A., and Field, K. G., 2017, "Sub-Size Tensile Specimen Design for in-Reactor Irradiation and Post-Irradiation Testing," *Nucl. Eng. Des.*, **320**(1), pp. 298–308.
- [5] Kasada, R., Takayama, Y., Yabuuchi, K., and Kimura, A., 2011, "A New Approach to Evaluate Irradiation Hardening of Ion-Irradiated Ferritic Alloys by Nano-Indentation Techniques," *Fusion Eng. Des.*, **86**(9–11), pp. 2658–2661.
- [6] Uchic, M. D., Dimiduk, D. M., Florando, J. N., and Nix, W. D., 2004, "Sample Dimensions Influence Strength and Crystal Plasticity," *Science*, **305**(5686), pp. 986–989.
- [7] Ozdemir, N., Karaman, I., Mara, N. A., Chumlyakov, Y. I., and Karaca, H. E., 2012, "Size Effects in the Superelastic Response of Ni54Fe19Ga27 Shape Memory Alloy Pillars With a Two Stage Martensitic Transformation," *Acta Mater.*, **60**(16), pp. 5670–5685.
- [8] Espinosa, H. D., Zhu, Y., and Moldovan, N., 2007, "Design and Operation of a MEMS-Based Material Testing System for Nanomechanical Characterization," *J. Microelectromech. Syst.*, **16**(5), pp. 1219–1231.
- [9] Kang, W., and Saif, M. T. A., 2010, "A Novel Method for In Situ Uniaxial Tests at the Micro/Nano Scale—Part I: Theory," *J. Microelectromech. Syst.*, **19**(6), pp. 1309–1321.
- [10] Kang, W., Han, J. H., and Saif, M. T. A., 2010, "A Novel Method for In Situ Uniaxial Tests at the Micro/Nanoscale—Part II: Experiment," *J. Microelectromech. Syst.*, **19**(6), pp. 1322–1330.
- [11] Oliver, W. C., and Pharr, G. M., 1992, "An Improved Technique for Determining Hardness and Elastic Modulus Using Load and Displacement Sensing Indentation Experiments," *J. Mater. Res.*, **6**, pp. 1564–1583.
- [12] Oliver, W. C., and Pharr, G. M., 2004, "Measurement of Hardness and Elastic Modulus by Instrumented Indentation: Advances in Understanding and Refinements to Methodology," *J. Mater. Res.*, **19**(1), pp. 3–20.
- [13] Ohmori, M., and Wakasa, K., 1973, "Tensile Ductility of Copper and Alpha-Brass Single Crystals at Elevated Temperatures," *J. Jpn. Inst. Met.*, **37**(11), pp. 1195–1199.
- [14] Zhao, Y. H., Guo, Y. Z., Wei, Q., Dangelewicz, A. M., Xu, C., Zhu, Y. T., Langdon, T. G., Zhou, Y. Z., and Lavernia, E. J., 2008, "Influence of Specimen Dimensions on the Tensile Behavior of Ultrafine-Grained Cu," *Scr. Mater.*, **59**(6), pp. 627–630.

- [15] Sun, J., Jin, L., Dong, J., Wang, F., Dong, S., Ding, W., and Luo, A. A., 2019, "Towards High Ductility in Magnesium Alloys—The Role of Intergranular Deformation," *Int. J. Plast.*, **123**(1), pp. 121–132.
- [16] Kassner, M. E., Nguyen, N. Q., Henshall, G. A., and McQueen, H. J., 1991, "The Effects of Temperature and Strain Rate on Extended Ductility of Aluminum," *Mater. Sci. Eng. A*, **132**(1), pp. 97–105.
- [17] Laporte, V., and Mortensen, A., 2009, "Intermediate Temperature Embrittlement of Copper Alloys," *Int. Mater. Rev.*, **54**(2), pp. 94–116.
- [18] Courtney, T. H., 2020, "Mechanical Behavior of Materials," 9781577664253: Amazon.Com: Books, <https://www.amazon.com/Mechanical-Behavior-Materials-Thomas-Courtney/dp/1577664256>, Accessed August 26, 2020.
- [19] Porollo, S. I., Dvoryashin, A. M., Ivanov, A. A., Konobeev, Y. V., and Shulepin, S. V., 2019, "Study of Phase-Structural Transformations Resulting in Low-Temperature Radiation Embrittlement in Ferritic-Martensitic Steel," *At. Energy*, **126**(1), pp. 39–45.
- [20] Takeda, Y., Kiattisaksri, C., Aramaki, M., Munetoh, S., and Furukimi, O., 2017, "Effects of Specimen Thickness in Tensile Tests on Elongation and Deformation Energy for Industrially Pure Iron," *ISIJ Int.*, **57**(6), pp. 1129–1137.
- [21] Sergueeva, A. V., Zhou, J., Meacham, B. E., and Branagan, D. J., 2009, "Gage Length and Sample Size Effect on Measured Properties During Tensile Testing," *Mater. Sci. Eng. A*, **526**(1), pp. 79–83.
- [22] Sun, X., Soulami, A., Choi, K. S., Guzman, O., and Chen, W., 2012, "Effects of Sample Geometry and Loading Rate on Tensile Ductility of TRIP800 Steel," *Mater. Sci. Eng. A*, **541**(1), pp. 1–7.
- [23] Yuan, W. J., Zhang, Z. L., Su, Y. J., Qiao, L. J., and Chu, W. Y., 2012, "Influence of Specimen Thickness With Rectangular Cross-Section on the Tensile Properties of Structural Steels," *Mater. Sci. Eng. A*, **532**(1), pp. 601–605.
- [24] Hogström, P., Ringsberg, J. W., and Johnson, E., 2009, "An Experimental and Numerical Study of the Effects of Length Scale and Strain State on the Necking and Fracture Behaviours in Sheet Metals," *Int. J. Impact Eng.*, **36**(10), pp. 1194–1203.
- [25] Dieter, G., 1986, *Mechanical Metallurgy*, McGraw-Hill Education, New York.
- [26] Oliver, D. A., 1928, "Proposed New Criteria of Ductility From a New Law Connecting the Percentage Elongation With Size of Test-Piece," *Proc. Inst. Mech. Eng.*, **115**(1), pp. 827–864.
- [27] 14:00-17:00, 2020, "ISO 2566-1:1984," ISO, <https://www.iso.org/cms/render/live/en/sites/isoorg/contents/data/standard/00/75/7524.html>, Accessed September 14, 2020.
- [28] Xu, X., Zhao, X., Ai, Y., Liang, M., Li, N., Lin, W., and Qin, C., 2020, "Study and Analysis on the Tensile Test Elongation Variation Law for High-Strength Pipeline Steel," *J. Mater. Eng. Perform.*, **29**(4), pp. 2164–2171.
- [29] Dhalla, A. K., and Winter, G., 1971, "Ductility Criteria and Performance of Low Ductility Steels for Cold-Formed Members," 1st International Specialty Conference on Cold-Formed Steel Structures, Aug. 20.
- [30] Goltsev, V. Y., Degadnikova, L. A., and Osintsev, A. V., 2017, "The Mechanical Testing of Materials Using the Method of Digital Image Correlation," 15th International School-Conference "New Materials – Materials of Innovative Energy (MIE)," Moscow, Russia, Oct. 23–27.
- [31] Thai, T. Q., Ruesch, J., Gratl, P. R., Truscott, T. T., and Berke, R. B., 2021, "Speckle Pattern Inversion in High Temperature DIC Measurement," Experimental Techniques.
- [32] Hild, F., and Roux, S., 2006, "Digital Image Correlation: From Displacement Measurement to Identification of Elastic Properties—A Review," *Strain*, **42**(2), pp. 69–80.
- [33] Hansen, R. S., Waldram, D. W., Thai, T. Q., and Berke, R. B., 2021, "Super Resolution Digital Image Correlation (SR-DIC): An Alternative to Image Stitching at High Magnifications," *Experimental Mechanics*, **61**(1), pp. 1351–1368.
- [34] Michael, A. M. A., Orteu, J.-J., and Schreier, H. W., 2009, "Digital Image Correlation (DIC)," *Image Correlation for Shape, Motion and Deformation Measurements: Basic Concepts, Theory and Applications*, H. Schreier, J.-J. Orteu, and M. A. Sutton, eds., Springer US, Boston, MA, pp. 1–37.
- [35] Salzbrenner, B. C., Rodelas, J. M., Madison, J. D., Jared, B. H., Swiler, L. P., Shen, Y.-L., and Boyce, B. L., 2017, "High-Throughput Stochastic Tensile Performance of Additively Manufactured Stainless Steel," *J. Mater. Process. Technol.*, **241**(1), pp. 1–12.
- [36] Hansen, R. S., Bird, T. J., Voie, R., Burn, K. Z., and Berke, R. B., 2019, "A High Magnification UV Lens for High Temperature Optical Strain Measurements," *Rev. Sci. Instrum.*, **90**(4), p. 045117.
- [37] Thai, T. Q., Smith, A. J., Rowley, R. J., Gratl, P. R., and Berke, R. B., 2020, "Change of Exposure Time Mid-Test in High Temperature DIC Measurement," *Meas. Sci. Technol.*, **31**(7), p. 075402.
- [38] Brlić, T., Rešković, S., Vodopivec, F., and Jandrić, I., 2018, "Lüders Bands at the Beginning of the Plastic Flow of Materials," *Metalurgija*, **57**(4), pp. 357–359.
- [39] Smith, A., 2021, "Development of a Variable Extensometer Method for Measuring Ductility Scaling Parameters," All Graduate Theses and Dissertations, Utah State University, Logan, UT.